Available online at www.sciencedirect.com
SCIENCE DIRECT®
Journal of Nuclear Materials 335 (2004) 14–32
journal of nuclear materials
www.elsevier.com/locate/jnucmat

Glass–ceramic nuclear waste forms obtained from SiO_2–Al_2O_3–CaO–ZrO_2–TiO_2 glasses containing lanthanides (Ce, Nd, Eu, Gd, Yb) and actinides (Th): study of internal crystallization

P. Loiseau [a], D. Caurant [a,*], N. Baffier [a], L. Mazerolles [b], C. Fillet [c]

[a] *Laboratoire de Chimie Appliquée de l'Etat Solide (UMR 7574), ENSCP, 11 rue Pierre et Marie Curie, 75231 Paris cedex 05, France*
[b] *CECM (UPR 2801) 15 rue Georges Urbain, 94407 Vitry-sur-Seine, France*
[c] *CEA, Direction de l'Energie Nucléaire, Centre de la Vallée du Rhône, DIEC/SCDV/LEBM, 30207 Bagnols-sur-Cèze, France*

Received 26 January 2004; accepted 18 May 2004

Abstract

Glass–ceramic waste forms such as zirconolite (nominally $CaZrTi_2O_7$) based ones can be envisaged as good candidates for minor actinides or Pu immobilization. Such materials, in which the actinides (or lanthanides used as actinide surrogates) would be preferentially incorporated into zirconolite crystals homogeneously dispersed in a durable glassy matrix, can be prepared by controlled crystallization (nucleation + crystal growth) of parent glasses belonging to the SiO_2–Al_2O_3–CaO–ZrO_2–TiO_2 system. In this work we present the effects of the nature of the minor actinide surrogate (Ce, Nd, Eu, Gd, Yb, Th) on the structure, the microstructure and the composition of the zirconolite crystals formed in the bulk of the glass–ceramics. The amount of lanthanides and thorium incorporated into zirconolite crystals is discussed in relation with the capacity of the glass to accommodate these elements and of the crystals to incorporate them in the calcium and zirconium sites of their structure.

PACS: 81.05.Kf; 81.05.Pj; 81.40.Ef

1. Introduction

Due to the ease of waste immobilization processes in glassy matrices (by melting and casting) and the high structural flexibility offered by such disordered materials, they are currently used (e.g. aluminoborosilicate glasses) to incorporate the broad range of high level radioactive wastes (HLW) – fission products + minor actinides – originating from the reprocessing of commercial or defense spent fuels. Nevertheless, because of both the higher chemical durability and the higher capacity of several single-phase ceramic matrices such as zirconates, titanates and phosphates [1–3] to incorporate specific nuclear wastes (corresponding either to a specific element or to a family of elements with similar chemical properties), ceramic waste forms have been proposed for the immobilization of long-lived radionuclides such as excess weapons plutonium and minor actinides.

* Corresponding author. Tel.: +33 1 44 27 67 08/24; fax: +33 1 46 34 74 89.
E-mail address: caurant@ext.jussieu.fr (D. Caurant).

0022-3115/$ - see front matter © 2004 Elsevier B.V. All rights reserved.
doi:10.1016/j.jnucmat.2004.05.020

Minor actinides could be separated from fission products of HLW by enhanced solvent extraction processes that would partition elements into chemically similar groups [4]. However, in comparison with glasses, the synthesis of ceramics in nuclear facilities remains generally more difficult to perform (pressing + sintering stages). Moreover, single-phase ceramic waste forms are not easy to prepare and low durability secondary phases able to incorporate significant amounts of radionuclides may form. The occurrence of both fluctuations in waste composition due for instance to incompletely separated actinides (if the performances of the wastes separation process are not as excellent as expected) and of impurities in plutonium wastes could also induce formation of uncontrolled parasitic phases. All these considerations indicate that glass–ceramics matrices can be envisaged as very interesting alternative waste forms for actinides immobilization. Indeed, such materials are easier to prepare than ceramics and are more tolerant to wastes composition variations (higher chemical flexibility) than ceramics due to the occurrence of a residual glass surrounding the crystals which can incorporate waste excesses and impurities unable to enter the crystalline phase [1]. The residual glass can also incorporate highly radioactive fission products (such as Cs) that can be added intentionally into the Pu-rich waste forms in order to discourage recovery of plutonium. Moreover, glass–ceramics exhibit higher thermal stability and better mechanical properties than glasses. If the long-lived radionuclides are mainly incorporated in the crystalline phase of the glass–ceramic waste forms, and if both crystalline and glassy phases exhibit very high chemical durability, these radionuclides will benefit from a double containment barrier and will be more efficiently isolated from the biosphere than in classical aluminoborosilicate nuclear glasses. However, only a few studies concerning glass–ceramics have been reported in literature as compared to the ones dealing with glasses and ceramics [1,5–8].

Minor actinides (Np, Am, Cm) are formed in nuclear reactors during fuel burn-up. They represent only a small weight fraction of HLW as compared to fission products (only 2–3 wt% of all the wastes in power reactors after Pu and U extraction). However, these long-lived radionuclides are mainly responsible for the long-term radiotoxicity (time > 300–500 years) of HLW obtained after spent fuel reprocessing. It can be noticed that Am and Cm show the highest contribution during approximately 10^5 years [9]. This is the reason why studies on advanced partitioning and specific immobilization of minor actinides in more durable matrices than current nuclear glasses are in progress in several countries such as France [4,9,10]. In nuclear glasses, minor actinides represent only about 0.4 wt% whereas concentrations of about 10 wt% are aimed to be immobilized in the new specific matrices.

In this work, we are concerned with minor actinides incorporation in zirconolite-based glass–ceramics consisting of zirconolite (nominally $CaZrTi_2O_7$) crystals homogeneously dispersed in a highly durable calcium aluminosilicate residual glass. Such waste forms can also be envisaged for Pu wastes immobilization and more particularly for low purity Pu wastes. However, because of the difficulties to manipulate highly active (α, γ) emitters in standard laboratories (preparation of waste form samples) and of the problems (extraction efficiency) that may occur industrially during the separation of the heaviest minor actinides (Am, Cm) from lanthanides (which represent more than 30 wt% of the HLW in power reactors), all experiments reported in this paper were performed using lanthanides (Ln) as non-radioactive actinides (An) surrogates due to their very close chemical properties [11]. This analogy between lanthanides and minor actinides is considered to be more accurate for the heaviest actinides Am and Cm for which high oxidation states are the less stable: as for lanthanides, Am and Cm mainly exit in their trivalent state in glasses and in zirconolite [12,13]. In this study, Pu^{3+}, Am^{3+} and Cm^{3+} ions were simulated by Ce^{3+}, Nd^{3+}, Eu^{3+} and Gd^{3+} ions because of their close ionic radii (Table 1). Moreover, as gadolinium is a very efficient neutron poison, it could advantageously be incorporated simultaneously with actinides in the zirconolite crystals of the glass–ceramics in the case of fissile actinides immobilization. A smaller lanthanide (Yb, which cannot be truly considered as a good actinides surrogate, see Table 1) has been also introduced in the glass–ceramics in order to investigate the influence of the lanthanide ionic radius on parent glass devitrification (nature, microstructure and structure of the crystalline phases formed) and on its incorporation into zirconolite crystals. Because of the possibility to prepare glasses and ceramics with both Ce^{3+} and Ce^{4+} ions, cerium is sometimes considered as a good plutonium simulant. Nevertheless, it must be underlined that cerium is easier to reduce in its trivalent state than plutonium when the preparation temperature of materials is raised and that in glasses prepared under air, plutonium is essentially in tetravalent state whereas both Ce^{3+} and Ce^{4+} ions exist in these conditions [15–17]. Neptunium exits mainly in +IV oxidation state in glasses melted under air [12,18,19] and in zirconolite ceramics [20]: It can be simulated by Ce^{4+} or Th^{4+} ions [11]. Moreover, thorium – which exits only in +IV oxidation state – is often considered as a good Pu^{4+} surrogate in spite of strong differences of solubility between Pu^{4+} and Th^{4+} in several ceramic matrices such as ZrO_2 [21]. Thus, in order to extend this study to both 5f and tetravalent ions, thorium has been introduced in one sample of zirconolite-based glass–ceramic as it is easy to handle due to its low radioactivity.

Table 1
Ionic radii of lanthanide and actinide ions in 6-, 7- and 8-fold coordinations from Shannon [14]

	Ca^{2+}	Zr^{4+}	Ce^{3+}	Ce^{4+}	Nd^{3+}	Eu^{2+}	Eu^{3+}	Gd^{3+}	Yb^{3+}	Th^{4+}	Am^{3+}	Cm^{3+}	Np^{4+}	Pu^{3+}	Pu^{4+}
Ionic radius in 8-fold coordination (Å)	1.12	0.84	1.143	0.97	1.109	1.25	1.066	1.053	0.985	1.05	1.09	–	0.98	–	0.96
Ionic radius in 7-fold coordination (Å)	1.06	0.78	1.07	–	–	1.20	1.01	1.00	0.925	–	–	–	–	–	–
Ionic radius in 6-fold coordination (Å)	1.00	0.72	1.01	0.87	0.983	1.17	0.947	0.938	0.868	0.94	0.975	0.97	0.87	1.00	0.86
(Ln, An)–O distance in 6-fold coordination (Å)	–	–	2.41	2.27	2.38	2.57	2.35	2.34	2.27	2.34	2.375	2.37	2.27	2.40	2.26
Field strength	0.35	0.89	0.46	0.78[a]	0.48	0.29[a]	0.52[a]	0.52	0.58	0.73	–	0.53	0.77	0.51[b]	0.79[b]
Z/d^2 ($Å^{-2}$)	(VI)	(VI)	(VIII)	(VI)	(VIII)	(VIII)	(VII)	(VII)	(VI)	(VI)	–	(VI)	(VI)	(VII)	(VII)
Literature reference	[73]	[74]	[75]		[76]			[77]	[77]	[78]		[79]	[18]	[17]	[75]

The 7- and 8-fold coordinations correspond respectively to the ones of the zirconium and calcium sites of zirconolite-2M. The values for cations in 6-fold coordination are given in order to enable the comparison of the ionic radii for all the lanthanide and actinide ions under the scope of this work. Field strength $F = Z/d^2$ was calculated for the different cations with Z cation charge and d cation–oxygen distance calculated as the sum of the cation and O^{2-} radii (with $rO^{2-} = 1.4$ Å [14]). The roman figures given under the F values correspond to the most probable cation site coordination in the parent glass estimated from literature data (EXAFS results on lanthanide and actinide doped glasses) and were used to calculate F. The (Ln, An)–O distances are also given for cations in 6-fold coordination calculated as the sum of the cations and O^{2-} radii to enable comparison with Ti–O distances in zirconolite (see text).

[a] In this case ionic radii were not available in [14] and F was calculated using the mean An–O distance determined by EXAFS in the corresponding references.

[b] In this case no EXAFS results were available in literature and the Ln coordination was estimated by analogy with other rare earths.

This paper presents the effect of the nature of minor actinides and plutonium surrogates on the crystallization processes in the bulk of SiO_2–Al_2O_3–CaO–ZrO_2–TiO_2 glasses. The nature, the structure and the composition of the crystalline phases formed after nucleation + crystal growth thermal treatments are determined. The amount of lanthanides and thorium incorporated in the zirconolite crystals (nominally $CaZrTi_2O_7$) formed in the bulk of the glass–ceramics is discussed in relation with the capacity of the glass to retain these elements and of the crystals to incorporate them in the calcium and zirconium sites of their structure. The effect of the nature of minor actinides and plutonium surrogates on the surface crystallization processes of these glasses will be presented in another paper [22].

2. Zirconolite ceramics wasteforms

Zirconolite was the most durable phase designed for the incorporation of actinides and lanthanides in Synroc phase assemblages developed in Australia in 1980s for immobilization of unpartitioned Purex-type HLW produced by the reprocessing of spent fuel [23]. More recently zirconolite-rich Synroc and zirconolite single-phase ceramics were also envisaged as specific matrix for Pu-rich waste [20,24,25] and minor actinides immobilization [10,26]. The long-term performances of zirconolite as actinides waste form are confirmed by the existence of very old natural samples which have incorporated and retained large amounts of UO_2 and ThO_2 in spite of metamictization phenomena due to radiation damages from α-decay [27–29]. Moreover, recent results showed that amorphization produced by external irradiation (Au^{2+} ions) did not significantly affect the dissolution rate of zirconolite [30].

Zirconolite (nominally $CaZr_xTi_{3-x}O_7$ with $0.83 \leqslant x \leqslant 1.36$ [31]) has a monoclinic layered structure (C2/c space group) referred as zirconolite-2M polytype consisting of alternate planes containing either Ti^{4+} ions or both Ca^{2+} and Zr^{4+} ions [31,32]. Calcium and zirconium ions are ordered within the planes in 8- and 7-fold coordinated sites, respectively. Titanium ions occupy three distinct sites, two of which (Ti(1) and Ti(3) sites) are 6-fold coordinated whereas the third (Ti(2) site), half-occupied, is 5-fold coordinated [32]. Zirconolite is well known for its excellent capacity to incorporate actinides and lanthanides ions into the Ca and Zr sites of its structure [24,33]. The preferential incorporation in Ca and Zr sites can be easily understood from ionic radius arguments (Table 1). It must be underlined that because of the small size of the Zr site, incorporation of lanthanides and actinides (in natural or artificial zirconolite samples) in this site is very limited in comparison with the amount of Ln and An that can be incorporated in

the Ca site without structural changes [28,34]. Four different incorporation Schemes (1)–(4) can be envisaged – if we exclude any vacancies in the structure – for trivalent (Ln^{3+}, An^{3+}) and tetravalent (Ln^{4+}, An^{4+}) lanthanides and actinides in the calcium and zirconium sites of zirconolite-2M:

$$\left[Ca^{2+}_{1-x}(Ln,An)^{3+}_{x}\right]_{Ca}[Zr^{4+}]_{Zr}\left[Ti^{4+}_{2-x}Al^{3+}_{x}\right]_{Ti}O_7, \quad (1)$$

$$\left[Ca^{2+}_{1-x}(Ln,An)^{4+}_{x}\right]_{Ca}[Zr^{4+}]_{Zr}\left[Ti^{4+}_{2-2x}Al^{3+}_{2x}\right]_{Ti}O_7, \quad (2)$$

$$\left[Ca^{2+}_{1-x/2}(Ln,An)^{3+}_{x/2}\right]_{Ca}[Zr^{4+}_{1-x/2}(Ln,An)^{3+}_{x/2}]_{Zr}\left[Ti^{4+}_{2}\right]_{Ti}O_7, \quad (3)$$

$$\left[Ca^{2+}\right]_{Ca}[Zr^{4+}_{1-x}(Ln,An)^{4+}_{x}]_{Zr}\left[Ti^{4+}_{2}\right]_{Ti}O_7. \quad (4)$$

Trivalent and tetravalent (Ln, An) cations incorporation in the divalent calcium site needs charge compensation with cations such as Al^{3+} in titanium sites (incorporation Schemes (1) and (2)). More precisely, we showed recently [35] by structure refinement (Rietveld refinement of X-ray diffraction diagram) of $Ca_{0.7}Nd_{0.3}ZrTi_{1.7}Al_{0.7}O_7$ (ceramic sample) that Al^{3+} ions mainly entered into the Ti(2) site of the structure. The preferential incorporation of aluminium ions in the 5-fold coordinated Ti site of zirconolite was confirmed recently by Vance et al. [36] for $Ca_{1-x}Y_xZrTi_{2-x}Al_xO_7$ ($0.1 \leqslant x \leqslant 0.3$) samples (Rietveld refinement of neutron diffraction diagrams).

The amount of (An, Ln) that can be incorporated in zirconolite-2M without structural changes (which means without new zirconolite-polytype, pyrochlore or perovskite formation for instance) strongly depends on its nature and more particularly on its cation radius. Incorporation Scheme (1) is the most efficient one. For instance, following this scheme, approximately 65% and 70% of the Ca^{2+} cations can be replaced respectively by Nd^{3+} and Gd^{3+} ions keeping the zirconolite-2M structure [37,38].

Nevertheless, in spite of its high capacity to incorporate An and Ln and its excellent long-term behavior, single-phase zirconolite waste forms remain more difficult to prepare either by sintering or by melting than glasses in nuclear facilities.

3. Previous works on glass–ceramics containing zirconolite crystals

To the best of our knowledge, preparation of glass–ceramic samples with zirconolite as the only crystalline phase in their bulk was reported for the first time by Fillet and co-authors [39,40]. These materials were developed in order to immobilize separated minor actinides. In their study, neodymium was used as trivalent minor actinides surrogate. Their parent glass composition belonged to the SiO_2–Al_2O_3–CaO–TiO_2–ZrO_2 system and the glass–ceramics were obtained by controlled thermal treatment of the parent glass. Using starting glass compositions close to the ones given in [39,40], the authors of this paper have studied bulk and surface crystallization processes (nucleation + crystal growth) in undoped and neodymium doped (up to 10 wt% Nd_2O_3) parent glasses [41–45]. For all these glass compositions, zirconolite was the only phase to crystallize in the bulk whereas a mixture of titanite (nominally $CaTiSiO_5$) and anorthite (nominally $CaAl_2Si_2O_8$) crystals grew from glass surface after heterogeneous nucleation and formed a thin crystallized layer. Using Energy Dispersive X-ray analysis (EDX), Electron Spin Resonance (ESR) and optical spectroscopy, Nd^{3+} ions were shown to enter preferentially the calcium site of zirconolite crystals (in the bulk of the glass–ceramics) and the calcium site of titanite crystals (in the surface crystallized layer). For these two crystalline phases, charge compensation was ensured by simultaneous incorporation of Al^{3+} ions in titanium sites [43,44]. These results partly justify the introduction of Al_2O_3 in the parent glass composition. The effect of crystal growth temperature T_c and parent glass composition on crystals microstructure, structure and composition was also studied. However the volume fraction X of zirconolite crystals formed in the bulk of the glass–ceramics using the parent glass composition studied in Refs. [39,40,44] was limited (X = 9–10 vol.% at T_c = 1200 °C). Leaching tests in aqueous solutions were conducted on similar glass–ceramic samples containing either neodymium or cerium as actinide surrogates [26,46,47]. Their results showed that the long-term release of actinide surrogates was governed mainly by the alteration of the residual glass remaining between zirconolite crystals in the bulk of glass–ceramics. However the overall chemical alteration of these waste forms remained very low in comparison with the one of nuclear borosilicate glasses and their long-term alteration rate was only one order of magnitude higher than the one of sintered zirconolite and two orders of magnitude lower than the one observed for the French SON68 borosilicate nuclear glass [26]. This good chemical durability is partly due to the occurrence of elements (Ti, Zr, lanthanides in both crystals and residual glass) with very low solubility in water.

4. Experimental procedures

Compositions (in mol.% and wt%) of the lanthanide and thorium-doped parent glasses prepared for this study are given in Table 2. A glass (G0) without actinides simulant was also prepared for comparison: SiO_2 (43.16), Al_2O_3 (12.71), CaO (20.88), TiO_2 (13.25), ZrO_2

Table 2
Composition (in oxide weight and molar percentage) of lanthanide- and actinide-doped parent glasses

Glass reference	Composition	SiO_2	Al_2O_3	CaO	TiO_2	ZrO_2	Ln_2O_3 or ThO_2	Na_2O
G0	wt%	43.156	12.709	20.884	13.249	9.002	0.000	1.000
	mol.%	48.848	8.477	26.328	11.282	4.968	0.000	1.097
GNd6	wt%	40.567	11.946	19.631	12.454	8.462	6.000	0.940
	mol.%	48.226	8.369	25.005	11.138	4.905	1.274	1.083
GNd4	wt%	41.430	12.201	20.049	12.719	8.642	4.000	0.960
	mol.%	48.439	8.406	25.116	11.188	4.927	0.835	1.088
GCe	wt%	40.627	11.964	19.660	12.472	8.474	5.862	0.941
	mol.%	48.226	8.369	25.005	11.138	4.905	1.274	1.083
GEu	wt%	40.567	11.946	19.631	12.454	8.462	6.000	0.940
	mol.%	48.253	8.373	25.019	11.145	4.908	1.218	1.084
GGd	wt%	40.567	11.946	19.631	12.454	8.462	6.000	0.940
	mol.%	48.270	8.376	25.028	11.149	4.910	1.183	1.084
GYb	wt%	40.155	11.825	19.431	12.327	8.376	6.956	0.930
	mol.%	48.226	8.369	25.005	11.138	4.905	1.274	1.083
GTh	wt%	40.567	11.946	19.631	12.454	8.462	6.000	0.940
	mol.%	48.058	8.340	24.918	11.099	4.888	1.617	1.080

(9.00), Na_2O (1.00) (in wt%). For each actinide surrogate, the following amounts (wt%): Ce_2O_3 (5.86), Nd_2O_3 (4.00 and 6.00), Eu_2O_3 (6.00), Gd_2O_3 (6.00), Yb_2O_3 (6.95), ThO_2 (6.00) were introduced to the basic glass composition G0 [43,44]. Rare earth molar concentrations for all samples (Table 2) were nearly similar to the one of the 6-wt% Nd_2O_3 doped glass (GNd6). This composition was widely studied in [43,44] and corresponded approximately to a 9.2 wt% Am_2O_3 doped glass which is closed to the amount of minor actinides aimed to be incorporated in such waste forms. However, because of the high atomic weight of thorium, Th molar concentration in glass GTh is close to the one of Nd in glass GNd4 (Table 2). All glasses (≈40 g) were prepared after thorough mixing of reagent grade oxide (SiO_2, Al_2O_3, ZrO_2, TiO_2, CeO_2, Nd_2O_3, Eu_2O_3, Gd_2O_3, Yb_2O_3, ThO_2) and carbonate ($CaCO_3$, Na_2CO_3) powders. The preparation method was the following:

- Melting under air in platinum crucible at 1550 °C for 10 h. For the cerium-doped glass, the melt was heated up to 1650 °C in order to displace the $Ce^{4+} \leftrightarrow Ce^{3+}$ equilibrium towards reduction (reduction is an endothermic reaction) to compare more easily the effect of cerium on glass crystallization with the other trivalent lanthanides of this study.
- Pouring in water and grinding in order to obtain more homogeneous glasses after a second melting.
- Second melting at 1550 °C for 4 h (1650 °C for the cerium doped glass) and casting in steel cylinders of 1.4 cm in diameter and height.
- Annealing at 775 °C (near glass transformation temperature range $T_g \approx 760$ °C determined as the onset of the DTA endothermic effect) and cooling to room temperature by switching off the furnace in order to relieve internal stresses before cutting.

It is interesting to note that contrarily to classical borosilicate nuclear glasses currently used for HLW immobilization and melted at temperatures never exceeding 1100–1200 °C, the absence of volatile products both in separated wastes or simulated ones and in parent glass batch (except a low amount of sodium used here only as chemical alteration tracer to perform chemical durability tests) allows higher melting temperatures in our case.

Glass–ceramics were then prepared by a two-step thermal treatment of parent glasses including a 2 h nucleation stage at $T_n = 810$ °C and a 2-h crystal growth stage at either $T_c = 1050$ or 1200 °C before annealing at 775 °C. Nucleation temperature was kept constant for all glass samples because T_g did not significantly change between the different compositions studied. Indeed, the temperature range where zirconolite nucleation remains significant was shown to be located only slightly higher than T_g [41]. Moreover the two crystal growth temperatures chosen in this study ($T_c = 1050$ and 1200 °C) were shown to lead to the crystallization of zirconolite as the only crystalline phase in the bulk of Nd-doped glasses [44].

All the samples were characterized by X-ray diffraction (XRD) using a diffractometer operating at CoKα wavelength ($\lambda K\alpha_1 = 1.78897$ Å). The bulks of glass–ceramics were studied by scanning electron microscopy (SEM) and energy dispersive X-ray analysis (EDX) on polished and carbon coated samples (accelerating voltage 15 kV, beam current ≈ 1.8 nA). For each glass–ceramic sample, the corresponding parent glass was used as reference for determination of crystals and residual glass composition by EDX. Such analysis were only performed for the glass–ceramic samples prepared at $T_c = 1200$ °C for which crystals were large enough to be probed by the microscope electron beam. A least six

measurements were performed and averaged for each phase and each sample. A fragment of the bulk of the thorium-doped glass–ceramic sample was also studied by high-resolution transmission electron microscopy (HRTEM) using an electron microscope working at 200 kV. Electron spin resonance (ESR) experiments were performed on several glass and glass–ceramic samples at room temperature (for Eu and Gd-doped samples) or at 12 K (for Yb doped samples) using a spectrometer operating at X-band ($\nu \approx 9.5$ GHz). Eu^{2+} and Gd^{3+} ions ($4f^7$ electronic configuration) are easily detected by ESR at room temperature due to the absence of spin-orbit coupling ($L = 0$) whereas Yb^{3+} ions ($4f^{13}$ electronic configuration) can be only detected at low temperature. Differential thermal analysis (DTA) was performed on 200 mg samples (particle size 125–250 μm) with a 10 °C/min heating rate in order to determine the glass transformation temperature T_g for the parent glass samples (determination method using the onset of the corresponding DTA endothermic effect).

In order to complete the structural characterization of the zirconolite crystals formed in the bulk of glass–ceramics, single-phase lanthanide and Th-doped zirconolite-2M ceramics were prepared by sintering under air as followed:

- Mixing and peletizing (2 t/cm^2) of reagent grade powders ($CaCO_3$, ZrO_2, TiO_2, Al_2O_3, Ln_2O_3, ThO_2).
- First sintering stage at 1400 °C for 100 h followed by grinding and peletizing.
- Second sintering stage at 1460 °C for 100 h. This second stage was performed in order to increase samples homogeneity.

The following zirconolite ceramic compositions were prepared: $Ca_{0.75}Ln_{0.25}ZrTi_{1.75}Al_{0.25}O_7$ (with Ln = Ce, Nd, Eu, Gd, Yb) and $Ca_{0.9}Th_{0.1}ZrTi_{1.8}Al_{0.2}O_7$. These compositions were close to the ones determined by EDX for the zirconolite crystals formed in the bulk of the different glass–ceramics heated at 1200 °C.

5. Results and discussion

5.1. Lanthanide and thorium-doped parent glasses

All the glasses prepared were easy to melt and no traces of crystalline phases were detected neither by microscopy nor by XRD. ICP-AES analysis performed at the CNRS laboratory of Vernaison (France) on the GNd6 glass showed good agreement between analyzed and theoretical glass compositions in spite of the high melting temperature (1550 °C). This can be explained by the lack of significant amounts of volatile compounds (Na_2O) in the melt.

5.1.1. Optical and ESR characterization of parent glasses

In some cases, the optical absorption and ESR characterization of the parent glasses can be of special interest to determine the simulant oxidation state. Glass G0 was uncolored but exhibited a strong and broad absorption band in the ultra-violet range with a maximum near 270 nm which could be due to the Ti^{4+}–O^{2-} charge transfer transition. As Th^{4+} ($5f^0$) ions are optically inactive, GTh glass remained uncolored, as expected.

Nd-doped glass samples showed the blue–purple coloration characteristic of Nd^{3+} ($4f^3$) ions f–f transitions: this is the most stable oxidation state of neodymium. Gd- and Yb-doped glasses are uncolored, which is consistent with the occurrence of the most stable trivalent oxidation state for Gd and Yb under normal conditions in air: Gd^{3+} ($4f^7$) ions absorb in the ultra-violet range whereas Yb^{3+} ($4f^{13}$) ions absorb in the near infra-red range. For example, the formation of Yb^{2+} (possible only for glasses melted under reducing conditions) would have been responsible for a strong absorption in the short wavelengths due to allowed f–d transitions.

Ce-doped glass (GCe) exhibited an amber coloration which cannot be explained neither by Ce^{4+} ($4f^0$) nor by Ce^{3+} ($4f^1$) f–f transitions. Ce^{4+} ions are optically inactive due to the lack of f-electrons but exhibit a charge transfer band from ligand oxygen in the ultra-violet range usually situated near 250 nm, whereas Ce^{3+} ions f–f transitions occurred only in the far infra-red range. Cerium is known to be easily reduced in its trivalent state in glasses melted at high temperature [15,48]. For instance using cerium L_{III} XANES spectroscopy, Lopez et al. [15] showed that the molar concentration ratio Ce^{3+}/Ce_{total} increased from about 0.5 to 0.9 when the preparation temperature of their cerium doped borosilicate glass increased from 1100 to 1400 °C. As the GCe glass was melted at 1650 °C, it can be assumed that cerium ions mainly exist as Ce^{3+} in our sample and that the coloration was due to trivalent cerium. In this case, the absorption band observed in the blue range with a maximum near 346 nm and a wide extension into the visible region for GCe glass could be due both to allowed interconfigurational Ce^{3+} ($4f^1 \rightarrow 4f^0 5d^1$) transitions and intervalence (charge transfer) transitions between Ce^{3+} and Ti^{4+} ions following the mechanism (Ce^{3+}, Ti^{4+}) → (Ce^{4+}, Ti^{3+}) [49]. This last mechanism – attributed to the occurrence of the Ce^{3+}–O–Ti^{4+} chromophore [49] – could occur in GCe glass because it contains high concentration of Ce_2O_3 (nearly 6 wt% Ce_2O_3) and more than 12 wt% TiO_2.

The glass GEu exhibited a yellow–orange coloration and had a wide absorption band with a maximum near 360 nm that cannot be attributed to intraconfigurational Eu^{3+} f–f transitions because such transitions are sharp and very weak (spin forbidden transitions). However, the coloration observed for GEu glass could be associated both to allowed interconfigurational f–d Eu^{2+}

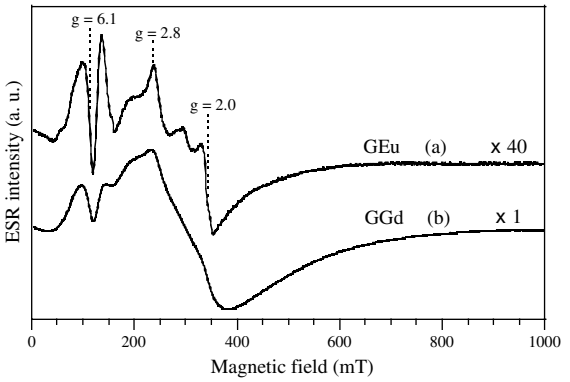

Fig. 1. X-band ESR spectra recorded at room temperature for GEu (a) and GGd (b) parent glasses (microwave power 20 mW, modulation amplitude 10 G, frequency 9.51 GHz). The effective g values of the three prominent features and the difference of magnification between the two spectra are indicated in the figure.

transitions ($4f^7 \rightarrow 4f^6 5d^1$) and to intervalence transitions between Eu^{2+} and Ti^{4+} ions: (Eu^{2+}, Ti^{4+}) $\rightarrow$ (Eu^{3+}, Ti^{3+}). The existence of a significant amount of Eu^{2+} ions in GEu glass was confirmed by ESR. As Eu^{3+} ions have a $^7F_0$ fundamental state, they cannot be detected by ESR (total angular momentum $J = 0$). However, as Eu^{2+} ions have a $^8S_{7/2}$ fundamental state (rare-earth S-state), they are easily detected by ESR at room temperature because of the lack of spin-orbit coupling (angular momentum $L = 0$). Fig. 1(a) gives the ESR spectrum recorded at room temperature of GEu glass, which is characteristic of Eu^{2+} ions in a low-symmetry site (with a distribution of crystal field parameters) [50]. This clearly shows that a significant amount of europium ions occurs in divalent state in GEu glass. In order to estimate the proportion of divalent europium in this glass, a method derived from the one described in [51] using the intensity of ESR spectrum of the Gd^{3+} doped glass (GGd) as standard (Fig. 1(b)) was applied (Gd^{3+} and Eu^{2+} ions have the same electronic configuration). After double integration of the ESR spectra, a Eu^{2+}/Eu_{total} molar ratio of approximately 3.5% was estimated. This relatively low amount of Eu^{2+} ions is thus responsible for the strong coloration observed. Consequently, for all the glasses prepared in this study, the rare-earth ions mainly exist in their trivalent state whereas thorium exists only as Th^{4+}.

5.1.2. Glass transformation temperature

The glass transformation temperature T_g for the different glasses was determined using DTA. It appeared that at least for the low Ln_2O_3 or ThO_2 molar concentration used in this study (0.8–1.6 mol.%), the identity of the minor actinide surrogate had no significant effect on T_g ($T_g \approx 760$ °C). It is interesting to notice that an increase of T_g with increasing atomic number (and thus decreasing ionic size) of the rare-earth ion was observed by Shelby [52] for glasses belonging to the SiO_2–Na_2O–Ln_2O_3 and SiO_2–Al_2O_3–Ln_2O_3 systems, but in this case rare-earth concentrations were higher (5–20 Ln_2O_3 mol.%) than in our study. Consequently, for the surrogate concentrations used in this work, the substitution of a rare earth by another one or even by thorium does not significantly affect the mean bond strength in the parent glasses.

5.2. Lanthanide and thorium-doped glass–ceramics

After heat treatment, all the glass–ceramic samples were totally opaque and exhibited different crystallization phenomena in their bulk (probably after homogeneous nucleation as described in [41]) and near their surface (heterogeneous nucleation). In this paper we present only the results concerning crystallization in the bulk.

5.2.1. Microstructure of zirconolite crystals

For the two crystal growth temperatures studied (1050 and 1200 °C), zirconolite was the only crystalline phase observed in the bulk of all the Ln- and Th-doped glass–ceramics for 2 h thermal treatment. This result is in accordance with the one we obtained for Nd-doped samples with Nd_2O_3 ranging from 0 to 10 wt% [45]. It can be noticed that the formation of Ln-containing silicate crystals such as lanthanide silicate apatite type phases – that were observed in several Ln-doped glasses [7] – has never been detected in our samples, probably because of the presence of ZrO_2 and TiO_2 in our parent glass compositions and of the relatively low Ln_2O_3 concentrations (Table 2).

5.2.1.1. SEM observations. Back-scattered SEM micrographs of the bulk of all the samples heat-treated at $T_c = 1050$ °C are shown in Fig. 2. It clearly appeared that the number of zirconolite crystals – and thus the zirconolite nucleation rate I_Z(Ln, Th) at $T_n = 810$ °C – strongly depended on the nature of the simulant: I_Z(Nd) < I_Z(Eu) < I_Z(Gd) < I_Z(Ce) < I_Z(Th) < I_Z(Yb). Ytterbium and thorium had the strongest enhancing effect on the nucleation rate. For the Ce, Nd, Eu or Gd-doped glass–ceramics heat treated at 1050 °C, the zirconolite crystals exhibited a dendritic shape already observed for the undoped (G0) and Nd-doped glass–ceramics [41,44]. For the Yb- and Th-doped samples, a high number of smaller crystals was observed. The growth of these ones was rapidly stopped during thermal treatment due to crystals impingement and residual glass depletion in ZrO_2 and TiO_2. At $T_c = 1200$ °C, the same kind of evolution between the different surrogates was observed (Fig. 3) but less clearly than at $T_c = 1050$ °C (probably because of the stronger ripening processes of zirconolite crystals at

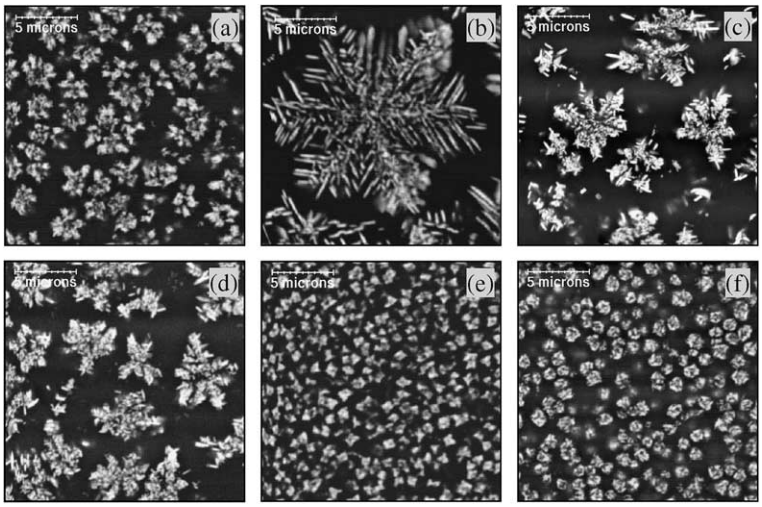

Fig. 2. Back-scattered SEM micrographs of the bulk of the glass–ceramics prepared after nucleation at 810 °C (2 h) and crystal growth at 1050 °C (2 h) from the glasses: GCe (a), GNd6 (b), GEu (c), GGd (d), GYb (e) and GTh (f). Magnification is the same one for all the images. The zirconolite crystals appear in white on the micrographs because of the high concentration of heavy elements (Zr, Ln, Th).

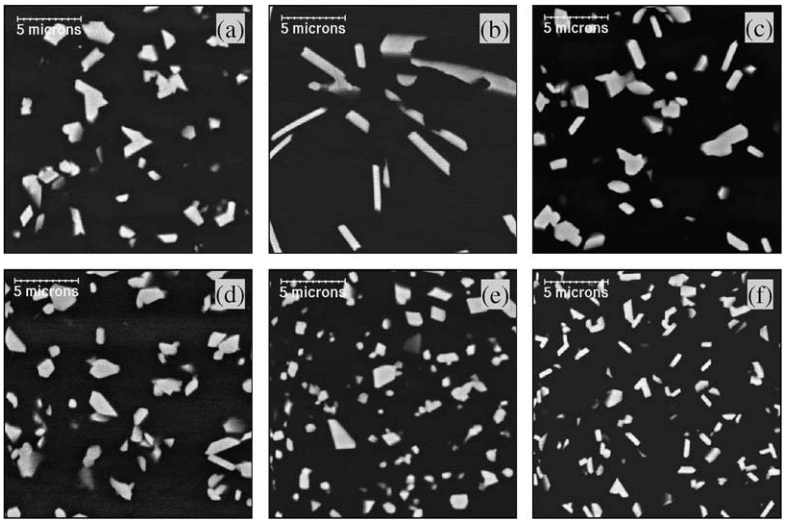

Fig. 3. Back-scattered SEM micrographs of the bulk of the glass–ceramics prepared after nucleation at 810 °C (2 h) and crystal growth at 1200 °C (2 h) from the glasses: GCe (a), GNd6 (b), GEu (c), GGd (d), GYb (e) and GTh (f). Magnification is the same one for all the images.

1200 °C due to the lower viscosity of the undercooled melt) and zirconolite appeared as more or less elongated crystals without clear dendritic shape. This microstructural evolution with T_c was explained in [44] for the Nd-doped glass–ceramics.

The amount of crystalline phase was estimated using SEM image analysis by area integration. Because of the dendritic shape of the crystals formed at $T_c = 1050$ °C, image analysis was only performed for the samples prepared at $T_c = 1200$ °C. In this case, it appeared that approximately 9–11 vol.% of zirconolite crystallized in the bulk, independently of the nature of the surrogate. We can notice that because of the nucleation stage which induced the formation of a high quantity of nuclei in the bulk, the size of the zirconolite crystals remains relatively small for all the samples and this particularly at $T_c = 1050$ °C (Fig. 2). This is very interesting for α-emitters immobilization in order to avoid glass–ceramics microfracturing due to radiation-induced crystals swelling [53]. Indeed, self-radiation studies performed on

^{244}Cm-doped zirconolite ceramics showed that macroscopic swelling could reach 6–7 vol.% [53].

5.2.1.2. Discussion on zirconolite nucleation rate. The results given above concerning the nucleation rate of zirconolite indicated that – except for the cerium-doped sample GCe – I_Z(Ln) strongly increased with decreasing the ionic radius $r(Ln^{3+})$ of the lanthanide trivalent ions from Nd to Yb (Table 1). Such an evolution can be partly explained by the increase of the rare-earth cation field strength F in the parent glass from Nd^{3+} ($F = 0.48$) to Yb^{3+} ($F = 0.58$) (Table 1). The cation field strength F was defined here as $F = Z/d^2$ for the different lanthanide and actinide cations with Z the cation charge and d the cation–oxygen distance calculated as the sum of the cation and O^- radii (with $rO^{2-} = 1.4$ Å [14]). The same observation concerning the evolution of I_Z can also be made for Th^{4+} ion that exhibits a strong field strength ($F = 0.73$). However, in spite of the higher field strength of Th^{4+} in comparison with Yb^{3+}, the effect of thorium on zirconolite nucleation rate was approximately the same as for ytterbium (Fig. 2). This result can be explained by the higher Yb molar concentration in parent glass GYb (Table 2).

A general correlation exists between the tendency of a modifier cation (as Ln^{3+} and Th^{4+} ions in our glass compositions) to separate from oxide glassy matrices and its field strength [54]: the higher its field strength (and thus the smaller the cation radius), the stronger its tendency to promote glass-in-glass phase separation and crystals nucleation in the bulk. This evolution is associated with the growing tendency of high field strength cations to compete for non-bridging oxygen (NBO) in the glassy network in order to satisfy their own environment: they have a strong tendency to separate in modifiers (as alkaline and alkaline-earth ions) and NBO-rich regions in the glass structure. This correlation also explains the role of nucleating agent well known for Zr^{4+} ($F = 0.89$ in 6-fold coordination [55]) and Ti^{4+} ($F = 1.10$ in 5-fold coordination [56]) ions in glass–ceramics [57–59]. In our case, the growing tendency of high field strength actinide surrogate ions to segregate simultaneously with Ti^{4+} and Zr^{4+} ions in modifiers (Ca^{2+} ions in our compositions) and NBO-rich regions of the glass structure could explain the increase of zirconolite nucleation rate. Indeed, all these cations (Ca^{2+}, Zr^{4+}, Ti^{4+}, Ln^{3+}, Th^{4+}) enter into zirconolite structure and their tendency to separate simultaneously in the glass could decrease the nucleation thermodynamic and kinetic barriers of zirconolite nuclei.

In spite of the small F value of Ce^{3+} ions ($F = 0.46$) in comparison with the other surrogates used in this study (Table 1), Fig. 2 showed that the zirconolite nucleation rate in GCe glass was higher than the one of Nd-, Eu- and Gd-doped samples. This apparently surprising result can be explained by the occurrence of a small amount of high field strength Ce^{4+} ions ($F = 0.78$) in the parent glass in spite of the high temperature used for its preparation (1650 °C). The cerium effect observed in this study can be correlated with the fact that Ce^{3+} ions are far more soluble than Ce^{4+} ions in oxide glasses [15]. On the contrary, because of the relatively low field strength of Eu^{2+} ions ($F = 0.29$), the occurrence of such ions did not increase zirconolite nucleation rate which remained controlled by Eu^{3+} ions ($F = 0.52$) in glass GEu.

5.2.2. Structure of zirconolite crystals

5.2.2.1. Lanthanide doped glass–ceramics. XRD patterns (Fig. 4) of the bulk of the glass–ceramics prepared either at 1050 or 1200 °C can all be indexed in the space group C2/c (zirconolite-2M polytype). This shows that the nature of the minor actinide surrogate did not modify neither the nature nor the structure of the crystals formed in the bulk. This underlines the good capacity of this glass–ceramic composition to incorporate surrogates with different cation radii. The unit cell parameters (a, b, c, γ) and the cell volume V were obtained from XRD data refinement. The evolutions of V and of a/b ratio versus $r(Ln^{3+})$ are shown in Fig. 5(a) and (c). For comparison, the evolution of the unit cell volume

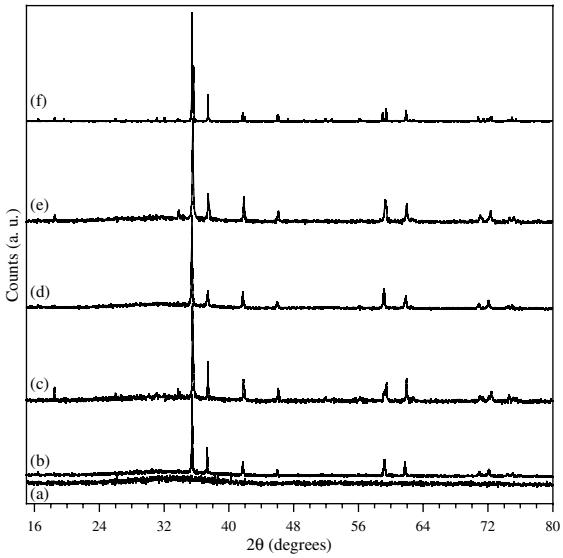

Fig. 4. XRD patterns of (a) Ce-doped parent glass, (b) bulk of the Ce-doped glass–ceramic prepared at $T_c = 1200$ °C, (c) bulk of the Yb-doped glass–ceramic prepared at $T_c = 1200$ °C, (d) bulk of the Ce-doped glass–ceramic prepared at $T_c = 1050$ °C, (e) bulk of the Yb-doped glass–ceramic prepared at $T_c = 1050$ °C, (f) $(Ce_{0.25})Zr(Ti_{1.75}Al_{0.25})O_7$ ceramic prepared at 1460 °C. All the patterns can be indexed in the space group C2/c (zirconolite-2M). For all the glass–ceramics, the contribution of the residual glass is also observed on the patterns ($\lambda CoK\alpha_1 = 1.78897$ Å).

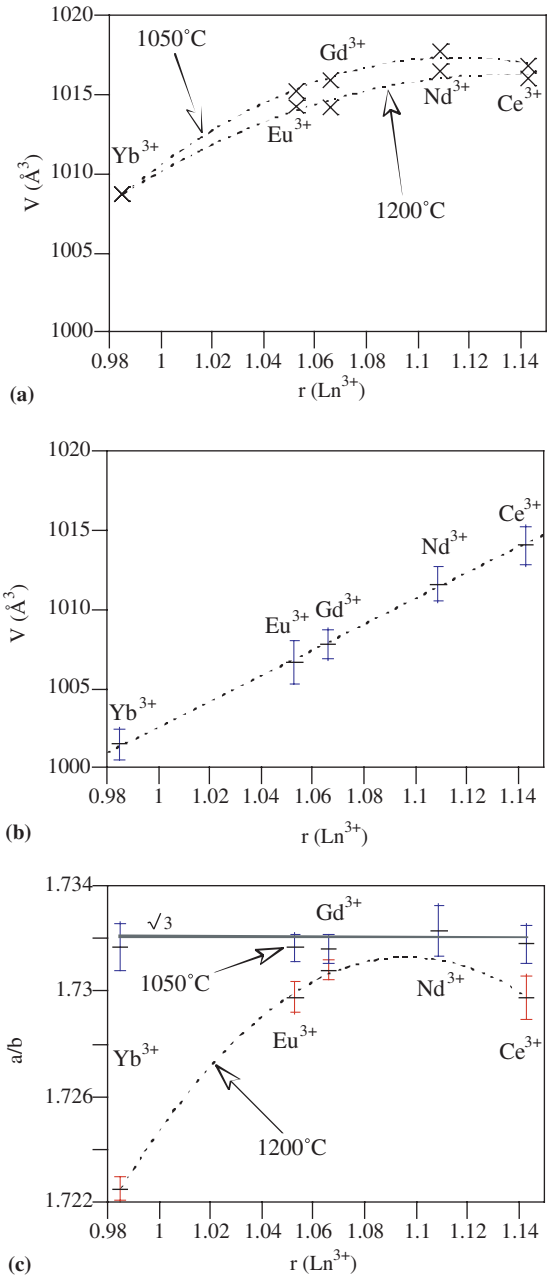

Fig. 5. Evolution versus Ln^{3+} radius of the cell volume V of zirconolite crystals in (a) the bulk of Ln-doped glass–ceramics prepared at $T_c = 1050$ and 1200 °C, (b) Ln-doped ceramics prepared at 1460 °C. (c) Evolution of the unit cell parameters a/b ratio of zirconolite crystals versus Ln^{3+} radius for the glass–ceramics prepared at $T_c = 1050$ and 1200 °C. $a/b = \sqrt{3}$ corresponds to a zirconolite-2M structure for which Ca^{2+} and Zr^{4+} ions are disordered in the planes of the structure with a high proportion of stacking faults along c^* [45].

V versus $r(Ln^{3+})$ of the Ln-doped zirconolite ceramics $(Ca_{0.75}Ln_{0.25})Zr(Ti_{1.75}Al_{0.25})O_7$ prepared at 1460 °C is given in Fig. 5(b). Comparison of Fig. 5(a) and (b) indicates that the evolution of the unit cell volume V of the zirconolite crystals formed in the glass either at 1050 or 1200 °C versus $r(Ln^{3+})$ follows the same trend as the one of the ceramics. This result is in accordance with the incorporation of rare-earth ions in zirconolite crystals – preferentially in the Ca site as in the ceramic samples – as shown below by EDX. However, differences are observed between zirconolite lattice parameters and unit cell volume for ceramics and glass–ceramics. This is partly due to the existence of differences between the composition of ceramics and glass–ceramics zirconolite crystals. As shown below in Table 4, the amount of rare-earth incorporated by formula unit in the zirconolite crystals ranges from $x = 0.13$ to 0.36 with decreasing $r(Ln^{3+})$. Moreover, the crystallinity of zirconolite crystals obtained by devitrification is worse than the one of zirconolite ceramics, which explained why the ceramics XRD lines are sharper and exhibit a more pronounced splitting. Notably, a strong disorder in the (Ca, Zr) planes of the structure was shown to occur for undoped and Nd-doped zirconolite crystals of the glass–ceramics prepared at 1050 °C [44]. The a/b ratio can be used to follow the ordering process with crystal growth temperature T_c: the closer to $\sqrt{3}$, the more disordered the Ca^{2+} and Zr^{4+} ions in their plane [40,60]. For all the Ln-doped glass–ceramic samples prepared at $T_c = 1050$ °C, Fig. 5(c) clearly indicates that zirconolite crystals remain strongly disordered independently of the nature of the lanthanide. At $T_c = 1200$ °C, the evolution of a/b versus r is more complex. For the small rare-earth ions, ordering of cations in the (Ca, Zr) planes is probably easier at 1200 °C than for the biggest ones, which could explain the high difference observed between the $a/b = f(r)$ curves corresponding to $T_c = 1050$ and 1200 °C (Fig. 5(c)). However for the biggest rare-earth ions, EDX results indicated (see below) that the amount of Ln^{3+} incorporated into the crystals was lower than for the smallest ones, whereas higher ordering diffusional problems are expected to occur (higher lanthanide cation radius). The contribution of these two opposite effects could explain the quite flat shape of the $a/b = f(r)$ curve at $T_c = 1200$ °C for the rare-earths belonging to the fist half of the series (Ce^{3+} to Gd^{3+}).

5.2.2.2. Thorium doped glass–ceramics. XRD patterns of the bulk of the Th-doped glass–ceramic heat treated at $T_c = 1050$ and 1200 °C are shown in Fig. 6. Contrarily to the Ln-doped samples, XRD patterns of the Th-doped one prepared at $T_c = 1200$ °C can be indexed either in the C2/c (zirconolite-2M) or in the $P3_12$ (zirconolite-3T) space groups (Table 3). The corresponding HRTEM image of a zirconolite crystal grown in sample GTh at $T_c = 1200$ °C is shown in Fig. 7(a). This image is composed of parallel domains with either 11.2 or 16.8 Å lattice fringes which extend without translational

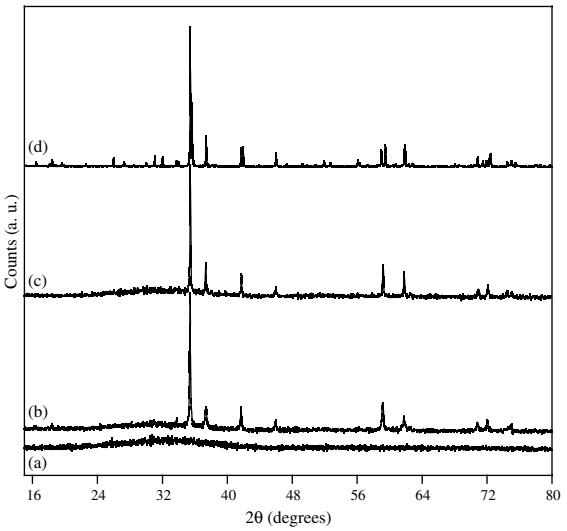

Fig. 6. XRD patterns of Th-doped parent glass (a); bulk of the Th-doped glass–ceramic prepared at T_c = 1050 °C (b) and 1200 °C (c); $Ca_{0.9}Th_{0.1}ZrTi_{1.8}Al_{0.2}O_7$ ceramic prepared at 1460 °C (d). For the two glass–ceramic samples, the contribution of the residual glass was also observed on the patterns. All the patterns can be indexed in the space group C2/c (zirconolite-2M). ($\lambda CoK\alpha_1$ = 1.78897 Å).

periodicity along c^* (c^* is the axis direction perpendicular to the Ti and (Ca, Zr) stacking planes). In accordance with HRTEM studies reported in literature on zirconolite polytypes [61], the occurrence of the 11.2 and 16.8 Å spacings in Fig. 7(a) is characteristic of respectively zirconolite-2M and -3T intergrowths. Consequently, the structure of the Th-doped zirconolite crystals formed in the bulk of the glass–ceramic is less regular than the one of Nd-doped samples for which HRTEM study had only revealed the occurrence of zirconolite-2M lattice fringes at 1200 °C as well as at 1050 °C [44]. On the other hand, the XRD pattern of the $Ca_{0.9}Th_{0.1}ZrTi_{1.8}Al_{0.2}O_7$ ceramic can only be indexed in the zirconolite-2M space group (Fig. 6(d)). This result was confirmed by HRTEM which showed only the existence of zirconolite-2M lattice fringes for the ceramic sample (Fig. 7(b)). It can be underlined that the formation of the zirconolite-3T polytype in the case of simultaneous incorporation of Th^{4+} and Al^{3+} ions in the structure (incorporation Scheme (1)) was reported in literature [62] when thorium concentration became sufficiently high. Th incorporation limit for which the phase change occurs between zirconolite-2M and -3T is much smaller ($x < 0.24$) than the one associated with phase change between zirconolite-2M and -3O polytypes for Nd- and Gd-doped ceramics ($x \geqslant 0.65$) [37,38]. This result concerning ceramics could explain the stronger tendency of the Th-doped zirconolite crystals formed in the glass–ceramic GTh to exhibit zirconolite-3T intergrowths in comparison with the rare-earth doped glass–ceramics.

Therefore, the occurrence of (Ca, Zr) disorder in the planes and the intergrowth of different polytypes in the zirconolite crystals formed after devitrification depends on the nature and on the charge of the surrogate introduced in the parent glass. The structure of these crystals is slightly different from the one of the ceramic samples. This last point can be due to a higher ceramic preparation temperature: 1460 °C for the ceramics in comparison with 1050 and 1200 °C for the glass–ceramics. This temperature difference could help ionic diffusion for structural ordering and more efficient dopant dispersion into the structure. Nevertheless, it is important to underline that the zirconolite-3T structure is not very different to the one of the 2M polytype: the cation sites remain almost identical for the two polytypes [63].

5.2.3. Composition of zirconolite crystals and study of (Ln, Th) incorporation

5.2.3.1. Lanthanide doped glass–ceramics

5.2.3.1.1. Composition of zirconolite crystals. The small size and dendritic shape of the zirconolite crystals

Table 3
Unit cell parameters and volume cell of the zirconolite crystals formed in the bulk of the Th-doped glass–ceramic samples prepared at T_c = 1050 and 1200 °C

Lattice parameters	T_c = 1050 °C (2 h)		T_c = 1200 °C (2 h)	
	C2/c	$P3_12$	C2/c	$P3_12$
a (Å)	12.555(5)	7.252(1)	12.548(2)	7.2439(4)
b (Å)	7.256(2)	7.252(1)	7.2437(9)	7.2439(4)
c (Å)	11.365(5)	16.767(5)	11.367(1)	16.758(2)
α (°)	90	90	90	90
β (°)	100.58(4)	90	100.61(1)	90
γ (°)	90	120	90	120
Cell volume (Å^3)	1018(9)	763.8(5)	1015(3)	761.6(2)

XRD patterns indexation was performed both in the C2/c (zirconolite-2M) and in the $P3_12$ (zirconolite-3T) space groups. Numbers in parentheses are standard deviations and apply to the last quoted place.

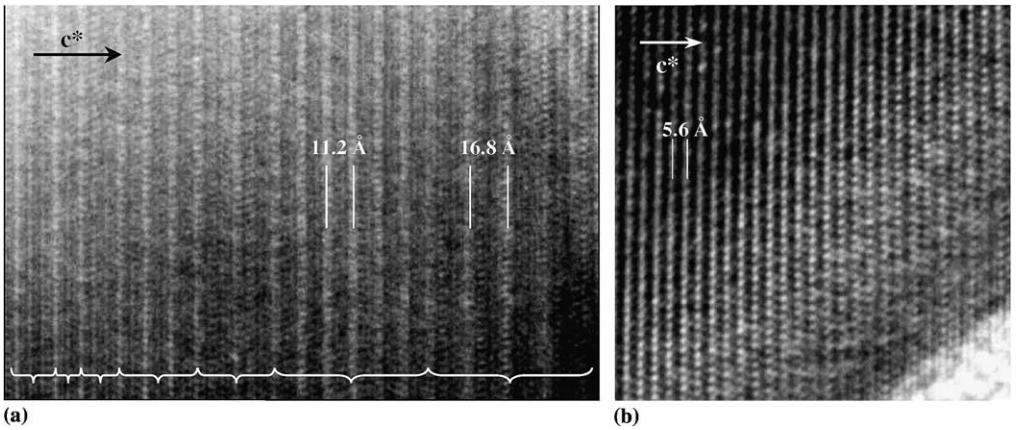

Fig. 7. HRTEM image of (a) a zirconolite crystal formed in the bulk of the Th-doped glass–ceramic prepared at T_c = 1200 °C, (b) the $Ca_{0.9}Th_{0.1}ZrTi_{1.8}Al_{0.2}O_7$ ceramic sample prepared at 1460 °C.

formed in the bulk at T_c = 1050 °C (Fig. 2) precluded EDX analysis without residual glass contribution to the X-ray spectra. Thus, only the larger crystals grown for 2 h at 1200 °C were analyzed by EDX (Fig. 3). The composition of the crystals obtained for the Ln- and Th-doped samples are given in Table 4. The evolution of the amount of rare earth and aluminum ions incorporated in the crystals versus Ln^{3+} radius is shown in Fig. 8. In the case of the Ln-doped glass–ceramics, it was assumed that all the simulants incorporated in the zirconolite crystals were in their trivalent state. Concerning cerium, both due to the high melting temperature of the parent glass GCe (1650 °C, see Section 5.1) and to the difficulty to displace – at lower temperature in the undercooled melt during crystal growth (for 2 h at T_c = 1050 or 1200 °C) – the equilibrium Ce^{3+}/Ce^{4+} established during melting towards oxidation (because of the very high viscosity of the melt in this temperature range which limits considerably oxygen diffusion), it will be assumed that the majority of cerium ions remains in trivalent state in the zirconolite crystals. ESR showed that both the concentration ratio $[Eu^{2+}]/[Eu^{3+}]$ and the environment of Eu^{2+} ions remain approximately the same for all the Eu-doped samples (parent glass and glass–ceramics). Consequently, it appears that the Eu^{2+} ions remain in the residual glass and do not enter into the zirconolite crystals. This result can be explained by the large cation radius of this ion in comparison with the ones of Eu^{3+}, Ca^{2+} and Zr^{4+} ions (Table 1).

Table 4 and Fig. 8 show that the amount of rare earth incorporated in the crystals progressively increases with decreasing Ln^{3+} ion radius from Ce^{3+} to Yb^{3+}. Comparison of the quantities of Ln^{3+} and Al^{3+} ions by zirconolite formula unit versus Ln^{3+} radius (Fig. 8) clearly indicates an increase of the difference between the amounts of lanthanide and aluminum incorporated in the crystalline phase from cerium to ytterbium.

Table 4
Composition determined by EDX for the zirconolite crystals formed in bulk of the lanthanide- and thorium-doped glass–ceramics for T_c = 1200 °C (2 h) (average of six analysis for each sample)

Parent glass	Zirconolite
GCe	$Ca_{0,86}Ce^{3+}_{0,13}Zr_{1,05}Ti_{1,81}Al_{0,15}O_7$
GNd	$Ca_{0,82}Nd^{3+}_{0,19}Zr_{1,05}Ti_{1,77}Al_{0,17}O_7$
GEu	$Ca_{0,78}Eu^{3+}_{0,25}Zr_{1,03}Ti_{1,75}Al_{0,19}O_7$
GGd	$Ca_{0,75}Gd^{3+}_{0,29}Zr_{1,04}Ti_{1,71}Al_{0,21}O_7$
GYb	$Ca_{0,69}Yb^{3+}_{0,36}Zr_{0,99}Ti_{1,70}Al_{0,26}O_7$
GTh	$Ca_{0,90}Th^{4+}_{0,09}Zr_{1,04}Ti_{1,77}Al_{0,20}O_7$

Trivalent state Ln^{3+} was assumed for all the Ln-doped samples (see text).

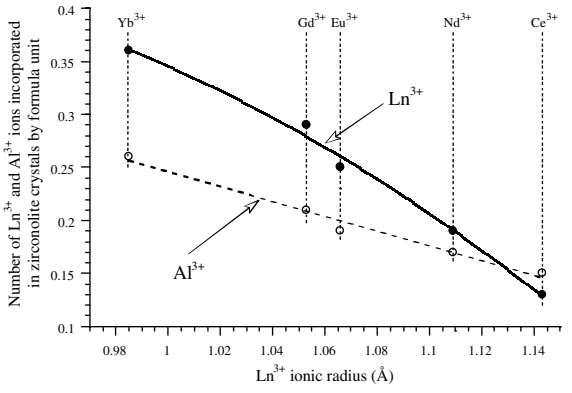

Fig. 8. Evolution of the lanthanide and aluminum amounts by formula unit (see Table 4) in the zirconolite crystals formed in the bulk of the Ln-doped glass–ceramics prepared at 1200 °C as a function of Ln^{3+} ions radius. For simplification reasons the radii [14] reported on the abscissa axis correspond to 8-coordinated Ln^{3+} ions (Ca site coordination in zirconolite).

Moreover, Fig. 8 shows that, except for the cerium-doped sample, the amount of aluminum – which are located in the titanium sites of zirconolite – is not sufficient to compensate the total positive charge excess induced by the incorporation of Ln^{3+} ions if these ones are only incorporated in the calcium sites of the zirconolite structure (incorporation Scheme (1)). This demonstrates that, at least for trivalent lanthanide cations smaller than Ce^{3+}, incorporation Scheme (3) operates. Thus, a fraction of the Ln^{3+} ions are simultaneously incorporated into both the Ca^{2+} and Zr^{4+} sites of the zirconolite crystals. Lanthanide cations are preferentially incorporated in the 8-coordinated calcium site and this amount increases with decreasing rare earth cation radius (see the curve associated with Al^{3+} in Fig. 8 which corresponds to the incorporation Scheme (1)). Moreover, the smaller the lanthanide size, the higher the amount of Ln^{3+} ions entering the Zr^{4+} sites (incorporation Scheme (3)). The progressive occurrence of simultaneous incorporation of actinide surrogates in both the calcium and zirconium sites was already observed in our previous works for neodymium-doped samples with increasing the Nd_2O_3 concentration in the parent glass and was confirmed by optical spectroscopy [45].

5.2.3.1.2. Discussion on lanthanide incorporation into zirconolite crystals. The evolution of the amount of Ln^{3+} ions incorporated in the zirconolite crystals formed in the bulk of the glass–ceramics (Table 4) can be explained considering both the capacity of the glass and of the crystals to accept these ions in their structures. Indeed, the partitioning of actinide surrogates between the residual glass and the zirconolite crystals is directly linked to their activity in these two phases: the amount of lanthanide ions incorporated in zirconolite results from the $[Ln^{3+}]_{\text{residual glass}} \leftrightarrow [Ln^{3+}]_{\text{zirconolite}}$ equilibrium at T_c.

Concerning the residual glass (or more precisely the undercooled melt coexisting with the crystals at T_c), the activity of Ln^{3+} ions probably increases with their field strength as indicated above. Therefore, the capacity of the residual glassy phase to incorporate lanthanide ions decreases with their size (Table 5 and Fig. 9). This tendency of the small rare earths to separate more easily from the glass has already been used above to explain the results concerning the nucleation rate I_Z. As a consequence, this could also partly explain the increase of the number of Ln^{3+} ions entering the Ca^{2+} and Zr^{4+} sites of the crystals (Fig. 8).

Concerning the zirconolite phase, the studies reported in literature about the incorporation limit of Ln^{3+} ions in zirconolite-2M ceramic samples showed that increasing rare earth amounts could enter the structure without phase changes following incorporation Scheme (3) with decreasing $r(Ln^{3+})$ [64]. For instance, results reported in literature for Gd- and Yb-doped ceramics prepared following incorporation Scheme (3) indicated that respectively $x = 0.24$ and 0.4 Ln^{3+} ions can be incorporated in zirconolite-2M [64]. Simple considerations about the radii of Ca^{2+}, Zr^{4+} and Ln^{3+} ions

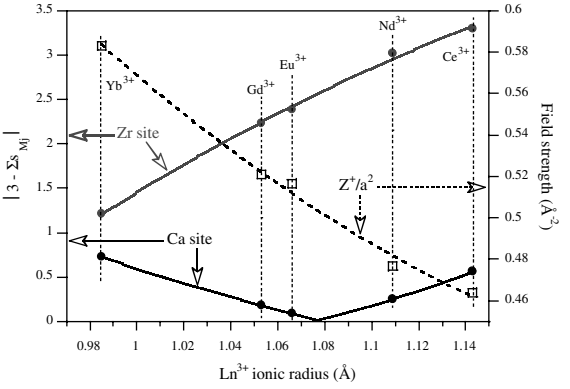

Fig. 9. Evolution of the Ln^{3+} ions field strength in the glass (Table 1) and of the difference $|\,3 - (\sum_j s_{Mj})\,|$ in the calcium and zirconium sites (Table 5) as a function of the lanthanide size.

Table 5
Sum of all the bond valences ($\sum_j s_{Mj}$) for M = Ln^{3+}, Th^{4+}, Ca^{2+} and Zr^{4+} ions surrounded by the j nearest oxygen neighbors in the calcium ($j = 8$) and zirconium ($j = 7$) sites of the zirconolite-2M structure

		Ce^{3+}	Nd^{3+}	Eu^{3+}	Gd^{3+}	Yb^{3+}	Th^{4+}	Ca^{2+}	Zr^{4+}
Ca site	$\sum s_{Mj}$	3.56	3.25	2.91	2.82	2.27	3.70	2.16	–
	$V_i - \sum s_{Mj}$	−0.56	−0.25	0.09	0.18	0.73	0.30	−0.16	–
Zr site	$\sum s_{Mj}$	6.60	6.02	5.39	5.23	4.21	6.90	–	
	$V_i - \sum s_{Mj}$	−3.60	−3.02	−2.39	−2.23	−1.21	−2.90	–	
	x	0.13	0.19	0.25	0.29	0.36	0.09	–	–

s_{Mj} was calculated using the formula (5) given in the text and the M–O distances were deduced from literature data for an undoped nearly stoichiometric $CaZr_{0.92}Ti_{2.08}O_7$ zirconolite-2M sample [68]. V_i is the oxidation state of the M cation and x corresponds to the number of Ln^{3+} or Th^{4+} ions by zirconolite formula unit for the glass–ceramics prepared at 1200 °C (Table 4).

(Table 1) show that zirconium sites are probably too small to accommodate high rare earth ions amounts except perhaps for the smallest ones such as Yb^{3+}. Concerning incorporation in the calcium site, it appears that the cation radius difference between Ca^{2+} and Ln^{3+} ions is smaller. This can explain the higher capacity of this site to incorporate rare earth ions. For instance, studies reported in literature showed that 65% and 70% of the Ca^{2+} ions can be replaced without phase change by Nd^{3+} and Gd^{3+} ions respectively in zirconolite-2M following incorporation Scheme (1) [37,38]. Consequently, all these considerations seem to indicate an increasing tendency of zirconolite crystals to accept Ln^{3+} ions when their size decreases.

However, a more precise approach using the calcium and zirconium sites geometry (Ca–O and Zr–O distances) in zirconolite is developed in this study to quantify the ability of these two sites to accept Ln^{3+} ions. The model used here is a combination of the Pauling's electrostatic valence principle [65] and of the empirical bond valence (s) – bond length (R) model developed by Altermatt and Brown [66] and Brese and O'Keefe [67]. According to this model, the sum of the bond valences s_{Mj} between a given cation M – such as Ln^{3+}, Th^{4+}, Ca^{2+} or Zr^{4+} in our case – and its j oxygen first neighbors is equal to its valence (or oxidation state) V_M in a stable structure: $V_M = \sum_j s_{Mj}$. Departure from this relation means that the corresponding M cation is either overbounded ($V_M \prec \sum_j s_{Mj}$) or underbounded ($V_M \succ \sum_j s_{Mj}$) to its oxygen neighbors, which means that the corresponding site of the structure is not well suited to incorporate cation M without important distortions. Consequently, the lower the difference $\Delta_M = |V_M - \sum_j s_{Mj}|$, the higher the expected solubility of M in the structure. The valences of the individual M–O bonds, s_{Mj} can be calculated from the bond lengths R_{Mj} (=distance between M and oxygen atom j) deduced from the zirconolite structure using the following relation:

$$s_{Mj} = \exp\left(\frac{R_0 - R_{Mj}}{B}\right), \tag{5}$$

where R_0 is the bond valence parameter of M and B is an universal constant equal to 0.37 Å [67]. R_0 values for different cations are tabulated in literature [66,67] and vary as a function of the cation's valence but not as a function of coordination number.

For this study, the Ca^{2+}–O^{2-} and Zr^{4+}–O^{2-} distances associated with the calcium and zirconium sites were deduced from Rietveld refinement of the XRD pattern of the undoped and nearly stoichiometric $CaZr_{0.92}Ti_{2.08}O_7$ ceramic [68]. These distances were used to calculate $\sum_j s_{Mj}$ for the different Ln^{3+} ions used in this study assuming their incorporation either into the calcium or into the zirconium site of zirconolite crystals. The values obtained are reported in Table 5 and are compared with $V_M = V_{Ln} = +3$. The evolution of $\Delta_M = \Delta_{Ln} = |3 - \sum_j s_{Mj}|$ as a function of Ln in the Ca and Zr sites is shown in Fig. 9. It clearly appears that the calcium site is much more suited to incorporate all the rare earth cations than the zirconium one. Moreover, the best suited Ln^{3+} ions to enter the Ca site are located approximately in the middle of the lanthanides series. Nevertheless, the associated differences $\Delta_{Ln}(Ca)$ for the Ca site remain low even for Ce^{3+} and Yb^{3+} ions in comparison with the corresponding values $\Delta_{Ln}(Zr)$ for the incorporation in the Zr site. Therefore, Ca^{2+} ions of the zirconolite-2M structure can be partly substituted by all the rare earths without strong structural distortions. It can be noticed that the $\Delta_{Ln}(Ca)$ values calculated for the Eu^{3+} (0.09) and Gd^{3+} (0.18) ions are close to the one associated with Ca^{2+} (0.16) in its own site (Table 5). Concerning the incorporation in the Zr site, ytterbium gives the lowest $\Delta_{Ln}(Zr)$ difference (Fig. 9), which means that Yb^{3+} ions enter more readily this site than the other rare earth ions studied in this work. This last result agrees both with the previous simple cation size considerations and with the data reported in literature concerning Gd and Yb solubility limits in zirconolite-2M following incorporation Scheme (3). Nevertheless, even for ytterbium, the difference $\Delta_{Ln}(Zr) = 1.21$ remains high. It is interesting to underline that the application of the bond valence-bond length model to Zr^{4+} ions in the zirconium site of zirconolite gives as expected the lowest value $\Delta_{Zr}(Zr) = |4 - \sum_j s_{Mj}| = 0.30$ in Table 5.

All previous considerations concerning the tendency of the small rare earths to both separate from the glass and to substitute for zirconium and calcium in zirconolite crystals can thus explain the experimental evolution reported in Fig. 8. In this case, the lower tendency of Yb^{3+} ion to substitute for Ca^{2+} ion in zirconolite shown by bond valence-bond length model (Fig. 9) is probably compensated both by its high capacity to enter the zirconium site and by its high tendency to separate from the residual glass (high field strength).

5.2.3.2. Thorium doped glass–ceramics. The composition of the zirconolite crystals formed at 1200 °C in the bulk of the Th-doped sample (Table 4) seems to indicate that Th^{4+} ions are preferentially incorporated into the Ca site following incorporation Scheme (2). In this situation, two Al^{3+} ions are needed for each Th^{4+} ion for charge compensation reasons. This result is in agreement with the analysis reported for thorium-rich zirconolite natural samples [28,69] for which Th^{4+} ions were shown to hardly substitute for Zr. For these natural samples, the charge compensation was ensured by Fe^{3+} and/or Mg^{2+} ions in Ti sites. However, artificial zirconolite-2M samples can be synthesized with 0.1–0.2 Th^{4+} ions by formula unit without charge compensator following incorporation Scheme (4). The preference of thorium for the Ca site in our glass–ceramics and in the

natural samples can be understood using the bond valence-bond length model. The bond valence sum $\sum_j s_{Thj}$ and the difference $\Delta_{Th} = |4 - \sum_j s_{Thj}|$ have been calculated for thorium in the calcium and zirconium sites (Table 5). The results obtained clearly confirm that thorium has a strong preference for the zirconolite Ca site in spite of the +2 charge excess.

Composition of the zirconolite crystals formed in the Th-doped sample can be compared to the one of the crystals formed in GNd4 glass–ceramic. The two corresponding parent glasses have similar simulant (Nd^{3+}, Th^{4+}) molar concentrations (Table 2). After crystallization (T_c = 1200 °C) of these two samples, the simulants are mainly incorporated in the Ca site but the amount of Nd in the zirconolite crystals is higher (Table 4) in spite of very close Δ_M(Ca) values (Δ_{Nd}(Ca) = 0.25, Δ_{Th}(Ca) = 0.30) and a higher Th^{4+} field strength in the glass (Table 1). This different behavior is due to the necessity to incorporate twice as many Al^{3+} ions in the Ti sites per Th^{4+} ion as for Nd^{3+}. This effect can be explained by the very high solubility of Al_2O_3 in the parent and residual glasses. Aluminum oxide acts as former oxide in silicate glasses where AlO_4^- entities participate with the SiO_4 tetrahedra to the glassy network and are charge compensated by Ca^{2+} ions.

In order to improve thorium incorporation in the zirconolite crystals of the glass–ceramics, Al_2O_3 concentration could be increased or other oxides such as MgO – acting as divalent charge compensator as in zirconolite natural specimens – could be added to the parent glass composition. In this situation, only one Mg^{2+} ion in Ti sites per Th^{4+} ion in Ca site would be necessary to ensure charge compensation. As Np^{4+} and Pu^{4+} ions have smaller size than Th^{4+} ion (Table 1), their activity in the glass and their capacity to substitute for Ca^{2+} and Zr^{4+} ions in zirconolite crystals should be higher. Therefore, the amount of plutonium and neptunium that would be incorporated in the crystalline phase could be significantly higher than for thorium.

5.2.4. Partitioning of Ln and Th between zirconolite crystals and residual glass

The composition of the residual glass in the bulk (between the zirconolite crystals) for the Gd- and Th-doped glass–ceramics prepared at T_c = 1050 and 1200 °C is given in Table 6. Zirconolite crystallization induces strong ZrO_2 and TiO_2 concentration depletions whereas SiO_2 and Al_2O_3 concentrations increase in the residual glass. The small increase of CaO concentration in the residual glass is due to the calcium excess in the parent glass in comparison with zirconolite stoichiometry $CaO:ZrO_2:2TiO_2$ (Table 2). Moreover, Table 6 indicates that the concentration of Gd in the residual glass decreases after crystallization. All the previous observations could also be made for Ce-, Nd-, Eu- and Yb-doped glass–ceramics (Fig. 10). For Th-doped samples, the thorium depletion in the residual glass is smaller than for Ln-doped glass–ceramics. This is in accordance with the crystals composition discussed above, which showed that the amount of Th^{4+} ions incorporated in the zirconolite crystals was the lowest (Table 4). Moreover, we can notice that when T_c decreases, the amount of TiO_2, ZrO_2, ThO_2 and Gd_2O_3 remaining in the residual glass also decreases. This can be explained by the formation of an increasing amount of zirconolite crystals for lower crystal growth temperatures in agreement with the results obtained for undoped and Nd-doped zirconolite glass–ceramics [41]. Correlatively, the Ln_2O_3 concentration remaining in the residual glass after zirconolite crystallization decreases with decreasing T_c. Moreover, the Ln_2O_3 depletion in the residual glass is stronger for the smallest rare earths in agreement with the increasing capacity of zirconolite crystals to incorporate Ln^{3+} ions with small radius (Table 4).

A partitioning ratio R, equal to the molar fraction of Ln^{3+} or Th^{4+} ions incorporated into the zirconolite phase versus the total simulant amount was calculated for the samples prepared at T_c = 1200 °C using a method developed in [70]. The results obtained are given in

Table 6
Compositions determined by EDX analysis for the residual glass remaining between the zirconolite crystals (T_c = 1050 and 1200 °C) in the bulk for Gd- and Th-doped samples

Composition (wt%)	SiO_2	Al_2O_3	CaO	TiO_2	ZrO_2	Gd_2O_3	ThO_2	Na_2O
GGd parent glass	40.57	11.95	19.63	12.45	8.46	6.00	–	0.94
Residual glass (T_c = 1200 °C)	43.80	15.90	22.20	8.06	3.83	5.21	–	0.99
Residual glass (T_c = 1050 °C)	47.92	17.41	22.87	4.84	1.90	4.10	–	0.96
GTh parent glass	40.57	11.95	19.63	12.45	8.46	–	6.00	0.94
Residual glass (T_c = 1200 °C)	44.30	14.59	21.32	8.38	4.11	–	6.12	1.18
Residual glass (T_c = 1050 °C)	46.26	15.13	21.71	6.73	3.60	–	5.35	1.22

The composition (wt%) given for the residual glass of the Th-doped glass–ceramic sample prepared at T_c = 1050 °C is only very approximative because of the high amount of very small zirconolite crystals (Fig. 2) which disturb the EDX analysis. The theoretical compositions of the corresponding parent glasses are also given.

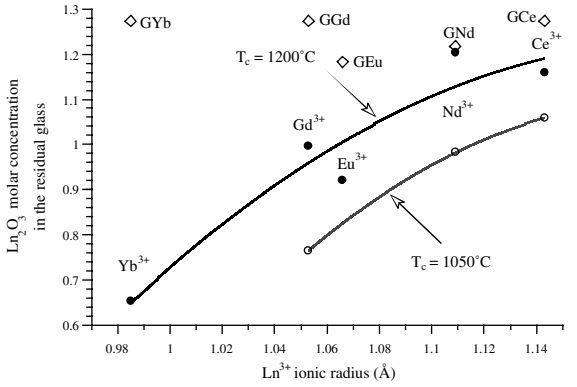

Fig. 10. Evolution of the Ln_2O_3 molar concentration determined by EDX analysis in the residual glass of the bulk of the glass–ceramics prepared at T_c = 1050 °C (○) and 1200 °C (●). For the Yb-doped sample prepared at 1050 °C, the very high density of zirconolite crystals precludes any glass analysis. For comparison, the Ln_2O_3 molar concentration (Table 2) in parent glasses is also given (◊).

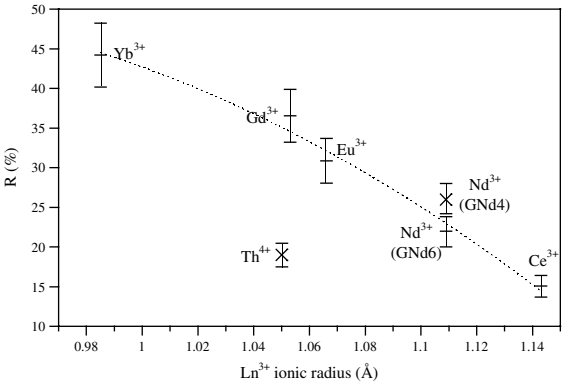

Fig. 11. Evolution of the partitioning ratio R of Ln^{3+} and Th^{4+} ions between the crystalline phase (zirconolite) and the residual glass in the bulk of the glass–ceramics prepared at T_c = 1200 °C versus cation radius (8-fold coordination). For neodymium, the R values corresponding to glasses GNd4 and GNd6 are given.

Fig. 11. This figure clearly shows that R strongly increases with decreasing the Ln^{3+} radius whereas the total amount of crystalline phase remains approximately the same (9–11 vol.%) for all the samples. For instance, the amount of simulant incorporated in zirconolite is three times as high for the Yb-doped sample as for the Ce-doped one. Approximately 45% of Yb^{3+} ions introduced in the parent glass composition are thus incorporated in the crystalline phase at T_c = 1200 °C. For the rare earth ions (Nd^{3+}, Gd^{3+}, Eu^{3+}) with radius closer to the ones of minor actinides, R ranges from 23% to 36% at this same temperature.

The R partitioning ratio ($R = 19 \pm 1.5\%$) for the Th-doped sample prepared at 1200 °C can be compared to the one of the GNd4 sample ($R = 26 \pm 2\%$) (Fig. 11). The smaller amount of thorium incorporated into the crystalline phase is in agreement with the EDX results reported in Table 4. However, for the tetravalent actinides occurring in nuclear wastes (Np^{4+}, Pu^{4+}) – which all exhibit smaller cation radius and thus higher field strength than thorium – R would be probably higher than for the Th-doped sample.

6. Conclusions

The aim of this work was to study the effect of the nature of minor actinide or Pu surrogates (Ce, Nd, Eu, Gd, Yb, Th) on the structure, the microstructure and the composition of the zirconolite crystals formed in the bulk of glass–ceramic samples prepared after nucleation and crystal growth of parent glasses belonging to the SiO_2–Al_2O_3–CaO–ZrO_2–TiO_2 system. The main conclusions that can be drawn from this work are the following:

(i) For all the surrogates, the corresponding parent glasses were easy to melt and were totally amorphous. The origin of the coloration observed for several samples was discussed. Optical absorption and ESR spectroscopies indicated that the rare earth cations were mainly in their trivalent state in the glass. However, for the europium-doped parent glass, a small quantity of Eu^{2+} ions ($[Eu^{2+}]/[Eu_{total}] \approx 3.5\%$) was detected by ESR.

(ii) For all the surrogates, zirconolite was the only crystalline phase to nucleate and to grow in the bulk of the glass after 2 h thermal treatment at either 1050 or 1200 °C. This clearly showed that the basic glass–ceramic composition chosen for this study could accept wide waste composition variations and more particularly could incorporate surrogates with different cation radii without changing the nature of the crystals. For this parent glass composition, the amount of crystalline phase formed in the bulk reached approximately 9–11 vol.% at T_c = 1200 °C for all the samples. Nevertheless, in accordance with our previous studies on Nd-doped samples [41,42], this volume percentage could be significantly increased by increasing ZrO_2 and TiO_2 concentrations in parent glasses. However, the nature of the dopant has a strong effect on the nucleation rate I_Z of the zirconolite crystals at 810 °C: $I_Z(Nd) < I_Z(Eu) < I_Z(Gd) < I_Z(Ce) < I_Z(Th) < I_Z(Yb)$. This evolution could be correlated with the increase of the cations field strength F in the undercooled melt. Indeed, except for the cerium-doped sample, $I_Z(Ln)$ strongly increased by decreasing the ionic radius $r(Ln^{3+})$ of the lanthanide trivalent ions from Nd to Yb ($F(Nd^{3+}) = 0.48$ and $F(Yb^{3+}) = 0.58$). The same observation concerning the

evolution of I_Z could also be made for Th^{4+} ions that exhibited a strong field strength ($F = 0.73$). Concerning the cerium doped glass–ceramic, the relatively high zirconolite nucleation rate could be explained by the occurrence of a small amount of high field strength Ce^{4+} ions ($F = 0.78$) coexisting with Ce^{3+} ions in the parent glass. This correlation between F and I_Z was in accordance with the tendency of high field strength modifier cations to separate from glassy matrices (increasing cation activity).

(iii) The crystals formed in the bulk at 1050 and 1200 °C for the Ln-doped samples corresponded to the zirconolite-2M polytype independently of the nature of Ln. The evolution of the crystals cell volume versus Ln was in agreement with the one determined for Ln-doped zirconolite ceramics. This showed that lanthanide cations were partly incorporated into the crystals. Moreover, XRD patterns clearly indicated that irrespective of the nature of Ln, a strong disorder occurred in the (Ca, Zr) planes of the zirconolite structure for the glass–ceramics prepared at 1050 °C. For the samples prepared at 1200 °C, ordering differences were observed between the different surrogates. In addition, occurrence of zirconolite-2M and -3T intergrowths were observed by HRTEM for the thorium doped sample. Nevertheless, due to the similarity between the structure of these two polytypes, these intergrowths would have probably no important effect concerning wastes immobilization.

(iv) EDX analysis of the zirconolite crystals grown at 1200 °C showed that at least for the trivalent lanthanide cations smaller than Ce^{3+} ions, a fraction of Ln^{3+} ions were simultaneously incorporated into both the Ca^{2+} and Zr^{4+} sites. Lanthanide cations were preferentially incorporated in the 8-coordinated calcium site (the charge compensation being ensured by the incorporation of Al^{3+} ions into the titanium sites) and this amount increased when the rare earth cation radius decreased. Moreover, the smaller the lanthanide size, the higher the proportion of Ln^{3+} ions entering the Zr^{4+} sites. This evolution of the amount of Ln^{3+} ions incorporated in the zirconolite crystals could be explained considering both the capacity of the glass (cation field strength) and of the crystals to accept these ions in their structures. An approach based on bond valence-bond length considerations was developed to quantify the ability of the calcium and zirconium sites of the zirconolite structure to accept Ln^{3+} ions. Concerning the thorium-doped glass–ceramic, it appeared that Th^{4+} ions were preferentially incorporated into the calcium site in agreement with Th-rich zirconolite natural samples, but its concentration in the crystals remained relatively low.

(v) The partitioning ratio R – defined as the molar fraction of Ln^{3+} ions incorporated into the zirconolite phase of the glass–ceramics – strongly increased with decreasing Ln^{3+} radius. Thus, for the smallest rare earth studied in this work (Yb), it was showed that approximately 45% of all the ytterbium ions were incorporated into the zirconolite phase for the sample prepared at 1200 °C. Due to the low Th incorporation level into the zirconolite crystals, the partitioning ratio for Th reached only 19% at the same preparation temperature.

In order to confirm the ability of the glass–ceramic matrix studied in this work to incorporate minor actinides or Pu wastes, samples using these radionuclides have to be prepared and studied. As a matter of fact, this confirmation was performed recently in the active Atalante laboratories (CEA-Marcoule, France) for ^{239}Pu-doped zirconolite-based glass–ceramics having the same composition as the ones studied in this paper but prepared by controlled cooling from the melt for technical reasons [71,72]. In this case, a strong Pu enrichment was observed in the zirconolite crystals.

References

[1] I.W. Donald, B.L. Metcalfe, R.N.J. Taylor, J. Mater. Sci. 32 (1997) 5851.
[2] R.C. Ewing, W.J. Weber, W. Lutze, in: E.R. Mertz, C.E. Walter (Eds.), Disposal of Weapon Plutonium, 1996, p. 65.
[3] L.A. Boatner, B.C. Sales, in: W. Lutze, R.C. Ewing (Eds.), Radioactive Waste Forms for the Future, Elsevier, Amsterdam, 1988, p. 495.
[4] C. Madic, M. Lecomte, P. Baron, B. Boullis, C. R. Phys. 3 (2002) 797.
[5] P.J. Hayward, Glass Technol. 29 (1988) 122.
[6] P.J. Hayward, in: W. Lutze, R.C. Ewing (Eds.), Radioactive Waste Forms for the Future, Elsevier, Amsterdam, 1988, p. 427.
[7] D. Zhao, L. Li, L.L. Davis, W.J. Weber, R.C. Ewing, Mater. Res. Soc. Symp. Proc. 663 (2001) 199.
[8] J.W. Wald, W.J. Weber, in: G.G. Wicks, W.A. Ross (Eds.), Nuclear Waste Management, Adv. Ceram., vol. 8, American Ceramic Society, 1984, p. 71.
[9] B. Boullis, in: R. Turlay (Ed.), Les Déchets Nucléaires, Les Editions de Physique, 1997, p. 69.
[10] C. Guy, F. Audubert, J.-E. Lartigue, C. Latrille, T. Advocat, C. Fillet, C. R. Phys. 3 (2002) 827.
[11] K.B. Krauskopf, Chem. Geol. 55 (1986) 323.
[12] R.G. Haire, N.A. Stump, Mater. Res. Soc. Symp. 465 (1997) 39.
[13] G.K. Liu, V.V. Zhorin, M.R. Antonio, S.T. Li, C.W. Williams, L. Soderholm, J. Chem. Phys. 112 (2000) 1489.
[14] Shannon, Acta Crystallogr. A 32 (1976) 751.
[15] C. Lopez, X. Deschanel, J.M. Bart, J.M. Boubals, C. Den Auwer, E. Simoni, J. Nucl. Mater. 312 (2003) 76.
[16] J.G. Darab, H. Li, M.J. Schweiger, J.D. Vienna, P.G. Allen, J.J. Bucher, N.M. Edenstein, D.K. Shuh, in: Topical Conference on Plutonium and Actinides, 25–27 August 1997, Santa Fe, New Mexico, Conference Transactions, p. 143.
[17] X. Feng, H. Li, L.L.D.L. Li, J.G. Darab, M.J. Schweiger, J.D. Vienna, B.C. Bunker, P.G. Allen, J.J. Bucher, I.M. Craig, N.M. Edelstein, D.K. Shuh, R.C. Ewing, L.M. Wang, E.R. Vance, Ceramic Trans. 93 (1999) 409.

[18] D. Petit-Maire, PhD thesis, Université Paris VI, France, 1988.
[19] I. Poirot, PhD thesis, Université Paris VI, France, 1986.
[20] B.D. Begg, E.R. Vance, S.D. Conradson, J. Alloys Compounds 271–273 (1998) 221.
[21] W.L. Gong, W. Lutze, R.C. Ewing, J. Nucl. Mater. 277 (2000) 239.
[22] P. Loiseau, D. Caurant, N. Baffier, C. Fillet, J. Nucl. Mater., submitted for publication.
[23] A.E. Ringwood, S.E. Kesson, K.D. Reeve, D.M. Levins, E.J. Ramm, in: W. Lutze, R.C. Ewing (Eds.), Radioactive Waste Forms for the Future, Elsevier, Amsterdam, 1988, p. 233.
[24] B.D. Begg, R.A. Day, A. Brownscombe, Mater. Res. Soc. Symp. Proc. 663 (2001) 259.
[25] A. Jostsons, E.R. Vance, D.J. Mercer, V.M. Oversby, Mater. Res. Soc. Symp. Proc. 353 (1995) 775.
[26] T. Advocat, P.J. McGlinn, C. Fillet, G. Leturcq, S. Schuller, A. Bonnetier, K. Hart, Mater. Res. Soc. Symp. Proc. 663 (2001) 277.
[27] G.R. Lumpkin, J. Nucl. Mater. 289 (2001) 136.
[28] R. Gieré, C.T. Williams, G.R. Lumpkin, Schweiz. Mineral, Petrogr. Mitt. 78 (1998) 433.
[29] G.R. Lumpkin, R.C. Ewing, B. Chakoumakos, R.B. Greegor, F.W. Lytle, E.M. Foltyn, F.W. Clinard, L.A. Boatner, M.M. Abraham, J. Mater. Res. 1 (1986) 564.
[30] K.L. Smith, Z. Zhang, P. McGlinn, D. Attard, H. Li, G.R. Lumpkin, M. Colella, T. McLeod, Z. Aly, E. Loi, S. Leung, M. Ridgway, W.J. Weber, S. Thevuthasan, Mater. Res. Soc. Symp. Proc. 757 (2003) 289.
[31] H.J. Rossell, J. Solid State Chem. 99 (1992) 52; Nature 283 1980 282.
[32] B. Gatehouse, I.E. Gray, R.J. Hill, H.J. Rossell, Acta Crystallogr. B 37 (1981) 306.
[33] E.R. Vance, D.K. Agrawal, Nucl. Chem. Waste Manage. 3 (1982) 229.
[34] H.J. Rossell, J. Solid State Chem. 99 (1992) 38.
[35] P. Loiseau, D. Caurant, N. Baffier, C. Fillet, Mater. Res. Soc. Symp. Proc. 757 (2003) 243.
[36] E.R. Vance, J.V. Hanna, B.A. Hunter, B.D. Begg, D.S. Perera, H. Li, Z.-M. Zhang, Environmental Issues and Waste Management Technology in the Ceramic and Nuclear Industries VIII, Ceramic Transactions 143 (2003) 313.
[37] E.R. Vance, C.J. Ball, R.A. Day, K.L. Smith, M.G. Blackford, B.D. Begg, P.J. Angel, J. Alloys Compounds 213&214 (1994) 406.
[38] E.R. Vance, A. Jostsons, R.A. Day, C.J. Ball, B.D. Begg, P.J. Angel, Mater. Res. Soc. Symp. Proc. 412 (1996) 41.
[39] C. Fillet, J. Marillet, J.L. Dussossoy, F. Pacaud, N. Jacquet-Francillion, J. Phalippou, Ceramic Trans. 87 (1998) 531.
[40] T. Advocat, C. Fillet, J. Marillet, G. Leturcq, J.M. Boubals, A. Bonnetier, Mater. Res. Symp. Soc. Proc. 506 (1998) 55.
[41] P. Loiseau, D. Caurant, O. Majerus, N. Baffier, C. Fillet, J. Mater. Sci. 38 (2003) 843.
[42] P. Loiseau, D. Caurant, O. Majerus, N. Baffier, C. Fillet, J. Mater. Sci. 38 (2003) 853.
[43] P. Loiseau, D. Caurant, N. Baffier, C. Fillet, Mater. Res. Soc. Symp. Proc. 663 (2001) 169.
[44] P. Loiseau, D. Caurant, N. Baffier, L. Mazerolles, C. Fillet, Mater. Res. Soc. Symp. Proc. 663 (2001) 179.
[45] P. Loiseau, D. Caurant, N. Baffier, C. Fillet, Proc. Phys. Chem. Glasses C 43 (2002) 195.
[46] P.J. McGlinn, T. Advocat, E. Loi, G. Leturcq, J.P. Mestre, Mater. Res. Soc. Symp. Proc. 663 (2001) 249.
[47] C. Martin, I. Ribet, T. Advocat, Mater. Res. Soc. Symp. Proc. 713 (2002) 405.
[48] J.M. Bart, A. Ribes, D. Rigaud, J.M. Boubals, F. Bart, C. Fillet, Ceramic Trans. 107 (2000) 665.
[49] A. Paul, Phys. Chem. Glasses 17 (1976) 7.
[50] C.M. Brodbeck, L.E. Iton, J. Chem. Phys. 83 (1985) 4285.
[51] D.L. Griscom, J. Non-Cryst. Solids 40 (1980) 211.
[52] J.E. Shelby, in: J.E. Shelby (Ed.), Key Engineering Materials (Rare Elements in Glasses), vols. 94&95, Trans. Tech. Publications, 1994, p. 1.
[53] W.J. Weber, R.C. Ewing, C.R.A. Catlow, T. Diaz de la Rubia, L.W. Hobbs, C. Kinoshita, Hj. Matzke, A.T. Motta, M. Nastasi, E.K.H. Salje, E.R. Vance, S.J. Zinkle, J. Mater. Res. 13 (1998) 1434.
[54] O.V. Mazurin, G.P. Roskova, E.A. Porai-Koshits, in: O.V. Mazurin, A. Porai-Koshits (Eds.), Phase Separation in Glass, Elsevier, Amsterdam, 1984, p. 108.
[55] G.E. Brown, F. Farges, G. Calas, Rev. Mineral. 32 (1995) 317.
[56] L. Cormier, G. Calas, P.H. Gaskell, J. Phys.: Condens. Matter. 9 (1997) 10129.
[57] P.W. McMillan, Glass–Ceramics, Academic Press, 1979, p. 61.
[58] Z. Strnad, in: Glass–Ceramic MaterialsGlass Science and Technology, vol. 8, Elsevier, Amsterdam, 1986, p. 72.
[59] A. Ramos, M. Gandais, J. Cryst. Growth 100 (1990) 471.
[60] E.R. Vance, C.J. Ball, M.G. Blackford, D.J. Cassidy, K.L. Smith, J. Nucl. Mater. 175 (1990) 58.
[61] T.J. White, Amer. Mineralogist 69 (1984) 1156.
[62] P.E. Fielding, T.J. White, J. Mater. Res. 2 (1987) 387.
[63] F. Mazzi, R. Munno, Amer. Mineral. 68 (1983) 262.
[64] H.J. Rossell, J. Solid State Chem. 99 (1992) 38.
[65] L. Pauling, J. Am. Chem. Soc. 51 (1929) 1010.
[66] D. Altermatt, I.D. Brown, Acta Crystallogr. B 41 (1985) 240.
[67] N.E. Brese, M. O'Keeffe, Acta Crystallogr. B 47 (1991) 192.
[68] R.W. Cheary, J. Solid State Chem. 98 (1992) 323.
[69] K.P. Hart, G.R. Lumpkin, R. Gieré, C.T. Williams, P.J. McGlinn, T.E. Payne, Radiochim. Acta 74 (1996) 309.
[70] P. Loiseau, PhD thesis, Université Paris VI, France, 2001.
[71] X. Deschanels, T. Advocat, T. Marcillat, J-M. Boubals, M. Bojat, in: Materiaux 2002 Proceedings, 21–25 October 2002, Tours, France.
[72] T. Advocat, T. Marcillat, X. Deschanels, G. Leturcq, F. Jorion, H. Rabiller, P. Loiseau, L. Veiller, in: C. Rabbe, E. Vernaz (Eds.), CEA Atalante: Rapport Scientifiifique 2002, Direction de l'énergie nucléaire (CEA-R-6800 ISSN 0429-3460), 2002, p. 144.
[73] G.E. Brown, F. Farges, G. Calas, Rev. Mineral. 32 (1995) 317.
[74] F. Farges, C.W. Ponader, G.E. Brown Jr., Geochim. Cosmochim. Acta 55 (1991) 1563.
[75] C. Lopez, PhD thesis, Université Paris XI, France (2002).

[76] S. Sen, J. Non-Cryst. Solids 261 (2000) 226.
[77] Y. Shimizugawa, J.R. Qiu, K. Hirao, J. Non-Cryst. Solids 222 (1997) 310.
[78] C.W. Ponader, G.E. Brown Jr., Geochim. Cosmochim. Acta 53 (1989) 2893.
[79] F. Farges, Geochim. Cosmochim. Acta 55 (1991) 3303.